

# Micro-structure mechanical failure characterization using rotating Couette flow in a small gap

Danny Blanchard, Phil Ligrani, Bruce Gale and Ian Harvey

Department of Mechanical Engineering, University of Utah, 50 South Central Campus Drive  
Rm. 2110, Salt Lake City, UT 84112, USA

Received 27 September 2004, in final form 19 January 2005

Published 25 February 2005

Online at [stacks.iop.org/JMM/15/792](http://stacks.iop.org/JMM/15/792)

## Abstract

A new method for testing the failure rates of micro-mechanical structures is presented. The technique uses Couette flow in a narrow-gap channel to induce different forces and loading on an array of structures. The Couette flow is induced by a rotating disc, which allows multiple devices to be tested at different designed stress levels depending on rotation speed and radial position. As an example, SU-8 micro-structures are used to present a general testing procedure that can be applied to other components. The forces acting on the micro-structures are due to fluid shear stress, centrifugal forces from rotation and form drag, all of which are characterized as they vary with radial position for one rotation rate. One series of tests with a single circumferential row of identical micro-structures is performed to determine the relative importance of these forces on revolutions to failure and failure rate of the structures in the row. Two additional series of tests are conducted to determine the effects of also adding unsteady loading from wakes to the structures. This unsteady loading from wakes is induced by time-varying velocity and pressure variations, which are imposed when additional rows of micro-structures are placed at smaller radial positions compared to the row being tested. Weibull failure rate approaches are used to provide information on failure rate as dependent upon cumulative revolutions. As such, the testing approach is useful for failure characterization of thin-film adhesion, self assembled nano-layers and micro-mechanical structures.

## Nomenclature

$C_d$	normalized drag coefficient
$H$	gap height between spinning disc surface and flat plate
$F_{D-C}$	total drag force for a cylinder in cross-flow
$F_{D-N}$	total drag force for tested micro-structures obtained from numerical flow predictions
$r$	radial position
$\mu$	dynamic viscosity
$\omega$	angular velocity

## 1. Introduction

The development of micro-fabrication technology has opened the door to the creation of micro-electro-mechanical systems (MEMS). These devices include a variety of sensors, actuators

and other devices. Reliability, failure analysis and strength characterization of device components are important for performance, useful to optimize fabrication processes and materials systems, and needed to predict failure modes and reliability.

Many different devices and techniques are employed to test the strength, fatigue and reliability characteristics of materials. Tensile testing is performed on bulk coupons using an Instron machine, an MTS machine or a micro-actuator [1–7], or by using a rotating substrate to apply centrifugal forces to test for tensile strength [8]. Shear testing can be performed by loading the end of a post with a probe [9]. Bending tests are performed by deflecting cantilever beams or membranes [10–12], bending the test material [13] or bending the substrate on which the specimen is bonded [14]. Torsional testing is performed on submicron single crystal silicon by

using an electrostatically actuated comb drive [15]. Adhesion tests are performed using a double cantilever, in which the two materials are ‘peeled’ apart [16]. These various tests and techniques are also applied to test the fatigue characteristics [1, 2, 4, 10, 11, 13] and reliability [5, 14].

In this work, a new test method is presented to apply well-defined forces and loading to micro-mechanical devices and structures. Forces are imposed on structures placed on a rotating disc using liquid-phase Couette flow in a narrow-gap channel. With this approach, multiple devices and arrays of structures can be tested at different stress levels depending upon the rotation speed and radial position on the disc. A Weibull-like approach to data analysis involves per cent failure of the array of micro-structures, as dependent upon revolutions to failure and averaged cycles to failure. Such data are presented as they vary with magnitudes and types of applied forces for the example architecture: SU-8 micro-structures on a stainless steel substrate. From these and other data, information on structure reliability, thin film adhesion and failure of system components is determined. The application of this technique to other micro-mechanical structures is discussed, and a generalized testing procedure is proposed. The proposed method has several advantages over current approaches, including the ability to test individual components or a whole integrated system. For example, multiple devices, at a variety of stress levels, can be tested at the same time (bulk testing), similar to procedures described by Ye *et al* [8]. The proposed approach is also advantageous because the use of fluid also eliminates the need for comb drives, or expensive equipment to apply forces to the tested device. As such, the test method is also ideal for testing roughness elements and protrusions [17], structures on the surface of a flow passage [18] and adhesion between micro-fabricated structures [19].

## 2. Test apparatus

The cross-section of the general test arrangement is shown in figure 1. The main components of this test apparatus are the shaft, test chuck, test housing, flat plate and the top of the test housing. The test chuck is constructed and then installed on the end of a shaft, as shown in figure 1. The shaft is made from stainless steel. One end of the shaft is 19.05 mm in diameter and is connected to the motor with a collet. The motor in all tests is the spindle of a three-axis milling machine. The middle of the shaft is 25.4 mm in diameter, with a diameter of 9.53 mm at the distal end. The test chuck is secured flush against this step in the shaft, as shown in figure 1, to allow repeatable repositioning of the chuck to within an accuracy of less than 20  $\mu\text{m}$ . The shaft also has a nylon bushing to reduce friction and heating of the shaft during operation.

The test chuck is 50.8 mm in diameter, 15.24 mm thick and is machined from a 304 stainless steel rod. One flat side is highly polished and the other side is drilled with a 9.53 mm hole to interface with the rotating shaft. The test chuck is mounted at a fixed distance away from a plexiglass flat plate. The test housing is constructed from a Lexan tube with 127 mm inner diameter. The flat plate on the bottom of the test housing is made from plexiglass. The top of the test housing is a piece of plexiglass with an o-ring to provide a seal with the Lexan tube, and a 25.4 mm hole for the shaft. The shaft is clamped

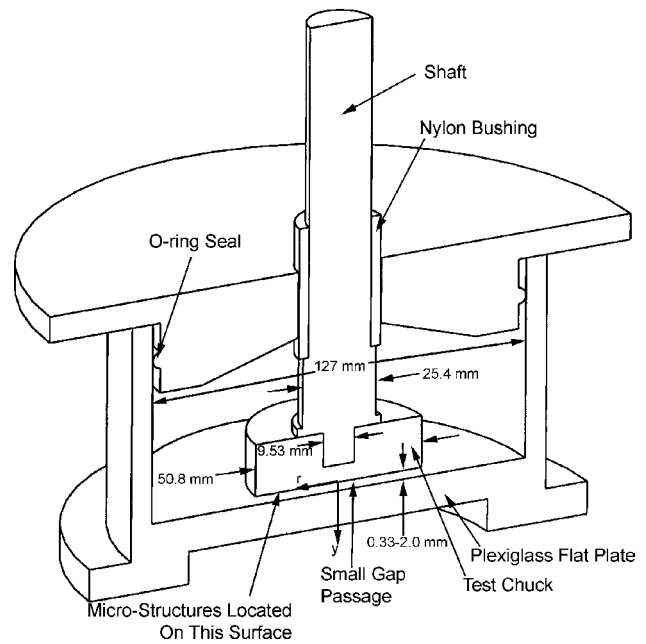


**Figure 1.** Cross-sectional view of test apparatus, with 50.8 mm diameter test chuck.

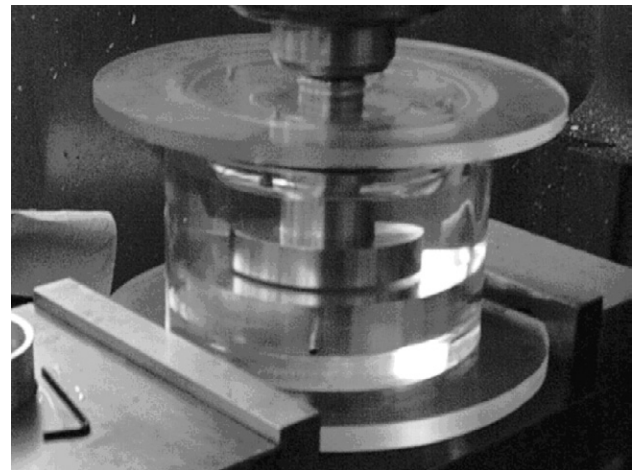


**Figure 2.** Photograph of test apparatus with test chuck spinning at 1000 rpm.

to a milling machine (which provides rotation). The fluid used for testing is soybean oil because it is viscous, transparent, inexpensive and readily available. The density and dynamic viscosity of the soybean oil are 914  $\text{kg m}^{-3}$  and 59  $\text{mPa s}$ , respectively [20]. Figure 2 shows a photograph of the test apparatus as a test is in progress.

## 3. Micro-structures tested

The materials used for the micro-structures and substrate are MicroChem SU-8 50 photopolymer and 304 stainless steel, respectively. SU-8 is chosen because it is regularly used in micro-fabricated structures, compatible with thick-feature photo-patterning, photopolymerizable and has good material properties and strength characteristics, which are given in table 1. Stainless steel is chosen as the substrate for

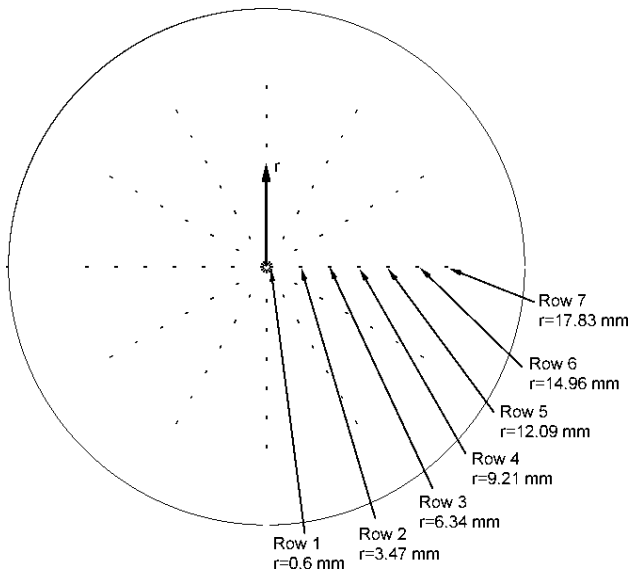


Figure 3. Micro-structure array configuration on the end of the 304 stainless steel rotatable test chuck.

Table 1. Material properties of SU-8.

Property	Value	Units	Reference
Young's modulus ( $E$ )	4.9	Gpa	[21]
Poisson's ratio	0.22	NA <sup>-1</sup>	[21]
Density	1.2	g cm <sup>-3</sup>	
Ultimate strength	120	Mpa	[22]
Maximum stress	34	Mpa	[21]

machinability and because it bonds well with the SU-8 photopolymer. The micro-structures are fabricated on the polished side of the test chuck using a photolithographic pattern and development process [23]. The length and height of the micro-structures are 290  $\mu\text{m}$  and 100  $\mu\text{m}$ , respectively, chosen based on numerical modeling to determine the thinnest structures with the most uniform stress distribution. The layout of the micro-structures on the test chuck is shown in figure 3. The micro-structure configuration consists of 12 radial columns. Each radial column contains seven circumferential rows (where row 1 is the inner row, and row 7 is the outer row). The inner edges of the micro-structures (at the smallest radii) are evenly spaced from radial positions of 0.6 mm (for row 1) to 17.8 mm (for row 7), as shown in figure 3. Note that there is an unused area between the edge of the test surface and the last row of structures, where slight irregularities in SU-8 height are typically present.

#### 4. Forces acting on the micro-structures

The principal forces acting on the micro-structures in the test set-up are from fluid shear stress, centrifugal forces from rotation and form drag. Unsteady loading to the structures is also present. This unsteady loading is induced by time-varying velocity and pressure variations, which are imposed when additional rows of micro-structures are placed at smaller radial positions compared to the row being tested.

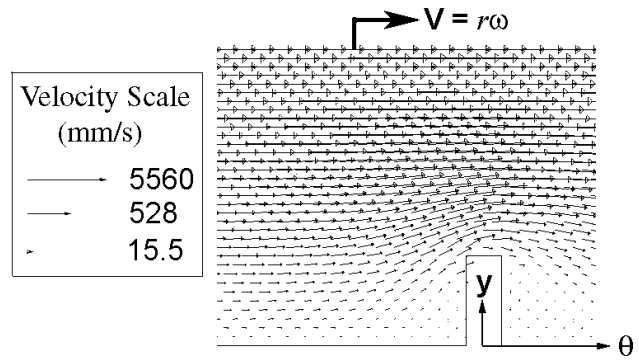


Figure 4. Numerically predicted flow vectors in a radial-circumferential plane around a segment of the small-gap circumferential flow passage in the vicinity of a single micro-structure.

With steady flow, and no micro-structures in the small-gap passage, the shear stress on the surface of the rotating disc with fully developed, rotating Couette flow is given by [24]

$$\tau = \frac{\mu\omega r}{H} \tag{1}$$

where  $\tau$  is the surface shear stress,  $\omega$  is the rotational speed of the disc,  $\mu$  is the viscosity of soybean oil,  $r$  is the radial location of the micro-structure and  $H$  is the gap height between the test chuck and the flat plate. This form of equation (1) requires the assumption that the circumferential velocity in the small gap passage is much greater than the radial velocity.

Numerical predictions of the Couette flow are made to determine the magnitudes of forces which are imposed on micro-structures placed on one wall of the small-gap passage. FLUENT version 6.1 is used for this purpose with steady laminar flow, and no unsteady loading due to passage of wakes induced by upstream micro-structures. For this effort, a two-dimensional cross-section of the flow with one single micro-structure is modeled. The total structure height to fixed wall gap size used in this model is 0.33 mm, and the rotational speed is 3000 rpm. For the boundary condition on the top wall, a velocity of  $r\omega$  is used. The moving top wall, bottom wall and micro-structure walls then have no-slip boundary conditions. The solver used is for laminar, two-dimensional flows. The inlet is a pressure inlet, and the outlet is a pressure outlet, both initialized with a gauge pressure of zero. The circumferential velocities and volumetric flow for these numerical predictions vary from row to row within the small gap passage. For row 1, the values are 117  $\text{mm s}^{-1}$  and 0.039  $\text{ml s}^{-1}$ , respectively, and for row 7, the values are 2824  $\text{mm s}^{-1}$  and 0.932  $\text{ml s}^{-1}$ , respectively. Each nodal element employed is 10  $\mu\text{m}$  wide, giving a total of 51 004 elements. An entry length of 9 mm is employed to ensure that fully developed Couette flow is present in the vicinity of the micro-structure. The resulting numerically predicted flow vectors in a radial-circumferential plane around a portion of the small-gap flow passage are shown in figure 4.

From this numerical analysis, forces from fluid shear are determined over the top surface area of the micro-structure. The pressure drag or form drag is estimated from the spatially averaged static pressure difference around the micro-structure. The forces from viscous drag and form drag are thus

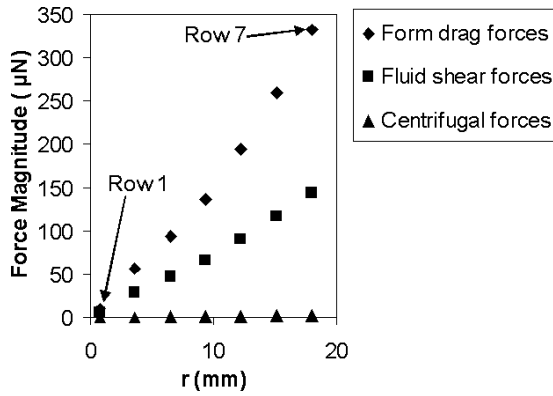


**Figure 5.** Analytically and numerically determined contributions from viscous forces, pressure form drag forces and centrifugal forces on a micro-structure as they depend upon radial position for a 0.33 mm small gap flow passage for a rotational test chuck speed of 3000 rpm.

**Table 2.** Reynolds number, total drag force for a cylinder in cross-flow and total drag force from numerical flow predictions over the tested micro-structure.

Row	$Re$	$F_{D-C}$ ( $\mu N$ )	$F_{D-N}$ ( $\mu N$ )
7	564	462.3869	475.9978
6	475	365.7019	376.355
5	384	278.4961	285.244

determined by multiplying the associated stresses by the area over which the stresses is acting. In both cases, these forces are estimated to be acting in the circumferential flow direction. The force due to centrifugal effects is the micro-structure mass multiplied by  $\omega^2 r$ . The resulting forces, as dependent upon radial position, are then given in figure 5 for a gap height of 0.33 mm, and a rotational speed of 3000 rpm.

Unsteady forces are estimated using a simplified fluid flow model of a cylinder in cross-flow to represent each micro-structure. The drag coefficient ( $C_d$ ) for a cylinder in cross-flow varies with Reynolds number and is dependent upon the resultant force parallel to the undisturbed initial velocity of the fluid, or the drag force [25]. This total drag force includes both viscous forces and form drag forces. Table 2 shows the total drag force from the numerical predictions from data in figure 5 ( $F_{D-N}$ ), and the experimental results for a cylinder in cross-flow ( $F_{D-C}$ ) reported by Schlichting [25]. The characteristic velocity and length used to calculate the Reynolds number in table 2 is the velocity of the micro-structure ( $r\omega$ ), and the height of the micro-structure, respectively. Because magnitudes of total drag force are in general agreement at different  $Re$ , the fluid flow model of a cylinder in cross-flow is used to estimate unsteady forces on the tested micro-structures.

There are two sources of unsteady forces on the micro-structures: (i) Karman vortex shedding [26, 27] and (ii) time-varying pressure and velocity variations due to the wakes of other micro-structures [28]. From the numerical study of Braza *et al* [26], average peak-to-peak fluctuation magnitudes of the normalized drag coefficient ( $C_d$ ) from Karman vortex shedding are estimated to be 0.2 for the range of Reynolds numbers used in the present work. Within the drag coefficient,

the drag force and fluctuations are normalized using the free stream velocity, fluid density and cylinder diameter. For the present study, the free stream velocity is defined as the local disc speed, and the cylinder diameter corresponds to the height of the micro-structure. A fluctuation of 0.2 in  $C_d$  corresponds to fluctuation magnitudes of the total drag force of 93  $\mu N$ , 65  $\mu N$  and 43  $\mu N$  for micro-structures on rows 7, 6 and 5, respectively. These fluctuation magnitudes are five times smaller than the total steady drag force. The frequency of the fluctuations in  $C_d$  is related to the Strouhal number [25, 27], with frequency values of 8 kHz, 10 kHz and 12 kHz for rows 5, 6 and 7, respectively.

The wakes behind the micro-structures may affect  $C_d$  as well as the magnitudes of drag coefficient oscillations [28, 29]. Nagai and Kurata [29] describe a reduction of  $C_d$  for downstream cylinders due to wake interference. King [28] also confirms this finding, and reports an increase in the amplitude of fluctuation of  $C_d$  by 20%. This decrease in  $C_d$ , and increase in fluctuations in  $C_d$  for downstream cylinders is also confirmed by Lam *et al* [30]. Thus, unsteady forces may affect the failure of the tested SU-8 micro-structures.

## 5. Testing procedures and conditions

For each of the three different test sequences, different numbers and radial positions of the micro-structures are employed to provide information on the effects of ‘cross-talk’ between different circumferential rows. For each particular arrangement of micro-structures, the rotational speed and gap height are varied to change the magnitudes of forces applied. Rotational speeds of 500–3000 rpm, and gap heights of 0.33–2.0 mm are used. The gap height is measured from the test chuck surface to the plexiglass flat plate, shown in figure 1, and is set using the three-axis milling machine with a precision of about 13  $\mu m$ . During testing, the test surface and the flat plate are parallel, with gap height variations less than 10  $\mu m$  across each radius. When a micro-structure array is tested, the stainless steel test chuck is first mounted to the motor shaft. Soybean oil is added to the test apparatus so that the test chuck is fully immersed. Any air bubbles are removed from the oil by rotating the test chuck at low rotational speed. The gap height is then set to the appropriate gap distance, and the test chuck is then rotated at the test speed for 1 to 2 min. The test surface micro-structures are then examined using an Edmund Industrial Optics computerized microscope with an A39-685 Infinivar CFM lens, the image from which is acquired using a Hitachi HV-C20 video camera. The signal from this camera is then acquired and digitized using a Matrox RT 2500 frame grabber card, installed within a Dell Computer 530 Workstation with a 2.40 GHz Intel Xeon processor. The positions and cycles to failure of all damaged micro-structures are then noted. The structures are considered to fail when part or all of the material is removed. The test procedures are then repeated, as required.

The first test series (test 1) is performed with seven circumferential rows of identical micro-structures mounted on the test chuck. The second test series (test 2) is conducted only with micro-structure rows 5, 6 and 7. These two different test series are designed to produce different magnitudes of unsteady loading on the micro-structures located in the seventh

circumferential row. The third test series (test 3) is performed only with row 7 to provide information on the effects of the forces induced by the Couette flow without the presence of flow disturbances from micro-structures located at smaller radii. The results for all three test series are obtained with a gap height of 0.33 mm at a rotational speed of 3000 rpm.

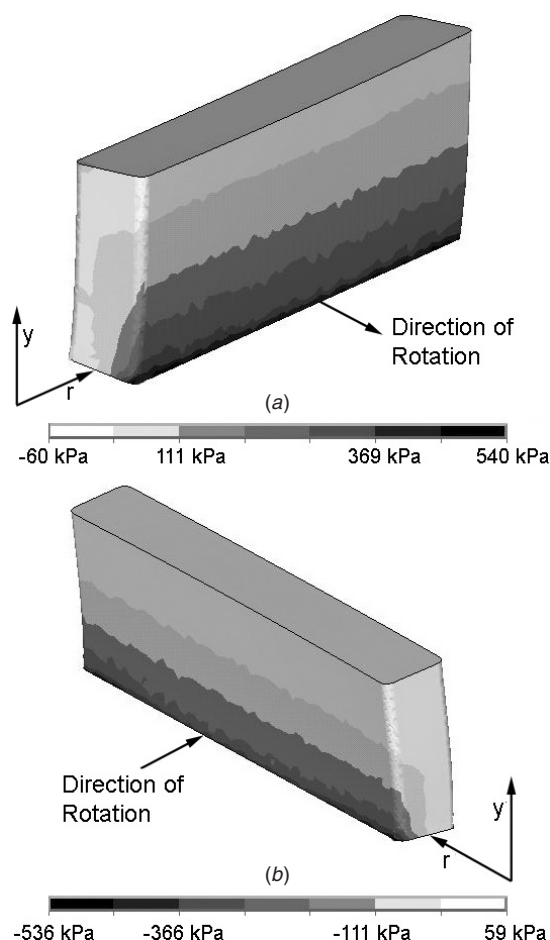
## 6. Results and discussion

Results from three series of tests are now discussed. In all cases, some form of physical micro-structure failure generally occurs between 12 000 and 120 000 cycles of rotation. Lower rotational speeds and larger gap heights give significantly lower failure rates, and are therefore not used to obtain the final results.

### 6.1. Numerical analysis of micro-structure stress distributions

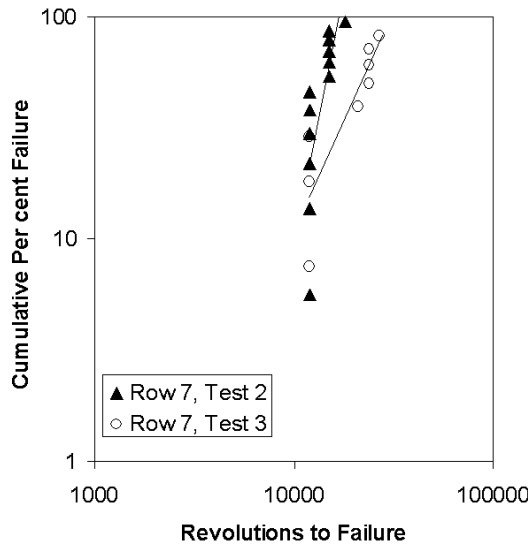
The ANSYS 6.0 numerical code is used to make numerical predictions of the stress distribution in micro-structures using nodal elements in a rectangular mesh. The numerical element type employed within this code is called SOLID 186, and is a three-dimensional 20-node structural element with quadratic displacement behavior. Each node within these elements has three degrees of freedom (translation in the  $x$ -,  $y$ - and  $z$ -direction). The micro-structure mesh employed is a hexagonal mesh with a maximum element length of  $6\ \mu\text{m}$ , giving a total of 42 841 elements and 63 259 nodes. Applied to the micro-structure are experimental magnitudes of centrifugal forces due to rotation, fluid shear forces and form drag. The fluid shear forces and form drag are calculated using Fluent 6.1 as described in section 4. Typical magnitudes as dependent upon radial position for a 0.33 mm gap flow passage for a rotational chuck speed of 3000 rpm are shown in figure 5. Centrifugal forces are imposed on the structure by employing the OMEGA command in ANSYS, which calculates the body forces due to rotation for a given material density, angular velocity and radial position of the micro-structure. The fluid shear force is imposed by applying forces on surface nodes on the top and sides of the micro-structure, such that the uniform fluid shear stress is equal to the sum of all the forces acting on the surface nodes divided by the area over which the surface nodes are distributed. The drag force is simulated by imposing a constant pressure boundary condition on the leading face of the micro-structure. Forces due to flow unsteadiness are not included in this analysis. The adhesion layer between the structure and the steel chuck is approximated by imposing a zero translational displacement (in the  $x$ -,  $y$ - and  $z$ -directions) boundary condition on the bottom of the structure. Seven complete rows of micro-structures are modeled as they rotate at 3000 rpm with a gap height of 0.33 mm. Each structure is rectangular in shape with  $5\ \mu\text{m}$  radius rounded fillets on the four corner edges, with height, length and width of  $100\ \mu\text{m}$ ,  $290\ \mu\text{m}$  and  $40\ \mu\text{m}$ , respectively. The inclusion of the fillets on the four corner edges lowers the stress concentrations by less than 10% compared to sharp corners at the edges.

Figure 6 shows the principal stress distribution for one structure on row 7. The magnitudes of the maximum stress concentrations are approximately 540 kPa for row 7, 430 kPa



**Figure 6.** Numerically predicted principal stresses distributed over the surface of a micro-structure on row 7 for test 3 for a test chuck rotational speed of 3000 rpm, and a small flow passage gap of 0.33 mm. Negative and positive values correspond to compression and tension respectively. (a) First principal stresses. (b) Third principal stresses.

for row 6 and 320 kPa for row 5. For the structure on row 7, figure 6 shows four stress concentrations located near the four corners of the micro-structure, and across the bottom of the leading and trailing edges of the micro-structure. The stress distribution is mostly a result of forces due to fluid shear stress and form drag, with insignificant contributions from centrifugal forces, which is consistent with figure 5. The maximum stress concentrations shown in figure 6 are less than the maximum tensile stress of SU-8 photoresist, which is 34 MPa [21], as well as the separation stress of SU-8 from silicon, which is 6.5 MPa [9]. The adhesion of SU-8 photoresist to stainless steel for the present structures is believed to be of similar magnitude. Also important is the consistency of the stress distribution in figure 6 with the SEM images of failed structures which are discussed later. In both cases, the results indicate that initial crack formation occurs near corners near locations where the SU-8 structures are bonded to the 304 stainless steel. The initial delamination located at one of the stress concentration is then followed by crack propagation and a brittle fracture of the photoresist structures.



**Figure 7.** Micro-structure failure data for row 7 from test 3 and for row 7 from test 2 for a test chuck rotational speed of 3000 rpm, and a small flow passage gap of 0.33 mm.

### 6.2. Effects of Couette flow forces on a single micro-structure row with and without unsteady loading due to wake interactions—comparison of tests 2 and 3

Percentage failure data as dependent upon the revolutions to failure are shown in figure 7 for row 7 from test 2 and for row 7 from test 3. The  $x$ -axis and  $y$ -axis in this figure are labeled ‘revolutions to failure’ and ‘cumulative per cent failure’ respectively, and are both scaled logarithmically. ‘Revolutions to failure’ is defined as the number of revolutions completed by the test chuck at the time of the failure of a micro-structure. ‘Cumulative per cent failure’ is defined as the cumulative per cent of failed structures from each row. Each point on the plot represents an initial failure of a micro-structure. The slope of such data provides information on the failure rate for a particular configuration. The rate of failure for test 3 is entirely a result of the forces imposed on the micro-structures from the small-gap, rotating Couette flow and unsteady forces due to vortex shedding. There are no micro-structures at smaller radii, and thus, no unsteady forces from the wakes of blades at inner radii. These forces are shown in figure 5 for test 3 arrangement, where centrifugal forces from rotation are two orders of magnitude less than the forces due to fluid shear stress and form drag. The largest of these forces at each radial position are due to form drag and fluid shear, along with the fluctuations due to the vortex shedding, which are then the most important contributors to micro-structure failure in test 3.

Comparing the results from tests 2 and 3 in figure 7 provides information on the influences of unsteady loading due to the wakes of micro-structures at smaller radii. This is because the micro-structures present in rows 5 and 6 in test 2 produce time-varying velocity and pressure variations as their wakes are advected past micro-structures located in row 7. Such unsteadiness is not present in test 3 because only one circumferential row of micro-structures is present in row 7. For the same percentage failure range, figure 7 shows that the revolutions to failure of micro-structures for row 7 from test 2

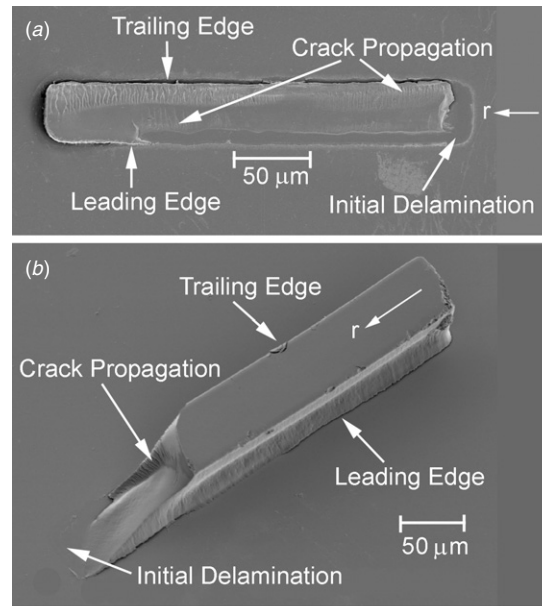


**Figure 8.** SEM photographs showing representative failure modes of micro-structures for a test chuck rotational speed of 3000 rpm, and a small flow passage gap of 0.33 mm. (a) Complete micro-structure fracture. (b) Partial micro-structure fracture.

are lower than values for row 7 from test 3. The failure rate (given by the slope) for test 3 is also lower than the failure rate for test 2. This is due to the effects of flow unsteadiness created by the micro-structures from rows at smaller radii for test 2. As discussed previously, the wakes from the inner radial structures reduce the average total drag force on the structures at larger radial locations, but also increase the periodic variation of total drag around each structure at larger radial locations. This occurs as the wakes from structures at inner radii are convected radially outward by secondary flows. Of importance are the cycle-to-cycle variations of this loading, in regard to both frequency and peak-to-peak magnitudes of the applied force variations. According to Khoo *et al* [9], the material response of the SU-8 photoresist is sensitive to the rate of loading and unloading, and an increase in magnitude and/or frequency of the unsteady loading has a significant effect on failure of the an SU-8 structure, which is consistent with the present data. Note that figure 7 also shows that the first micro-structure to fail from tests 2 and 3 occurs for about the same number of revolutions to failure.

A Hitachi S-3000N variable pressure scanning electron microscope (SEM) with a tungsten electron source and an Oxford Inca EDX microscope system is used to image the micro-structures after testing to provide information on the failure modes and mechanisms. These are generally obtained after a number of the micro-structures in a particular row have failed. Figures 8(a) and (b) show top views of typical failures. Note that the micro-structure in figure 8(a) is pointing to the rotational center of the test chuck at its right end, and shows a near-complete failure. Figure 8(b) shows a partial fracture of a micro-structure. Also observed are delaminations of micro-structures from the stainless steel chuck, and fractures that initiate near the central portions of the structures. According to these and other observations, typical failures start with an

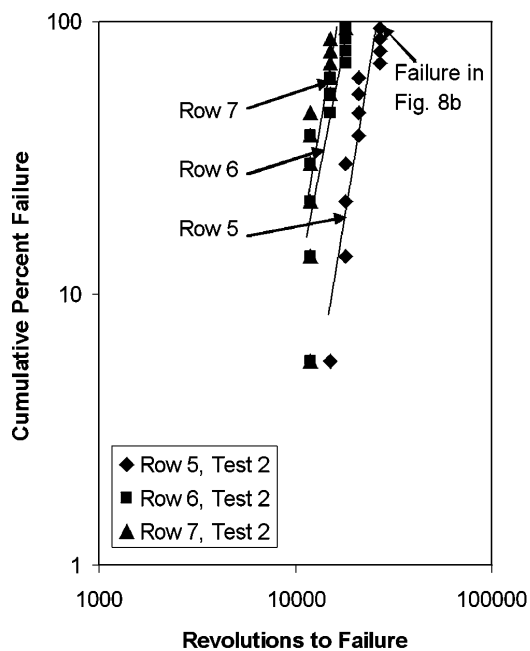


**Figure 9.** Micro-structure failure data for rows 5, 6 and 7 from test 2 for a test chuck rotational speed of 3000 rpm, and a small flow passage gap of 0.33 mm.

initial delamination initiating from one of the corners, where stresses are concentrated, followed by crack propagation, and then, a brittle fracture of the SU-8 photoresist micro-structures. Crack propagation, which appears to be present in most of the failed structures, occurs either near the boundary of the SU-8 and the stainless steel, or within the central portions of the structures. In some cases, such crack propagation suggests the presence of manufacturing defects that create a path favorable to crack growth [9]. Possible manufacturing defects include incomplete cross-linking of the SU-8 photoresist structure, incomplete bonding of the SU-8 to the substrate in a few areas of the micro-structure and residual stresses from micro-fabrication.

### 6.3. Effects of unsteady flow forces on micro-structure rows—results of test 2

Test 2 employs micro-structures in circumferential rows 5, 6 and 7 to illustrate the effects of flow unsteadiness on per cent failure and revolutions to failure. For this arrangement, the additional unsteadiness is provided by the velocity and pressure variations from micro-structure wakes which originate in row 5 and then affect structures in rows 6 and 7. Velocity and pressure variations from micro-structure wakes also originate in row 6 which then provide unsteady loading to the structures in row 7.

Figure 9 shows that the micro-structures are failing in the order that is predicted using a simple stress analysis based only on micro-structure position. The slopes, as related to failure rate (and as determined from the data-fit straight lines), also are about the same magnitude for rows 5, 6 and 7. These failure rates are also related to the rates and directions of crack propagation, fabrication variations and possible initial manufacturing defects. The partial overlap of the data in figure 9 for data from rows 6 and 7 in test 2 also suggests

similar unsteady loading and stress application rates for the structures located in these two rows. This is because both of these rows are influenced by the loading applied by the unsteady wakes which originate in row 5. As discussed previously, the unsteady wakes decrease the mean total drag force, but increase the average peak-to-peak fluctuations of the total drag force. The increased fluctuations in stress due to the unsteady form drag and shear fluid loading, and the cyclic nature of the unsteady loading, appears to cause delamination, local crack propagation and then faster failure rates as the cyclic loading is underway. The combination of this and the other applied forces then causes brittle fracture when the crack reaches a critical size [31]. Thus, the same failure mechanism mentioned earlier is present, fatigue crack growth, followed by fracture of the structure. This is consistent with the results shown in figures 8(a) and (b). Note that the data point associated with the structural failure shown in figure 8(b) is identified in figure 9. Crack initiation at the adhesion layer between the SU-8 photoresist and the 304 stainless steel substrate may also play a role in this process, according to the results given by Khoo *et al* [9], who report delamination of SU-8 photoresist from a silicon substrate when the shear stress at the interface reaches 6.5 MPa.

### 6.4. Effects of rows 1–4 on micro-structure failures in rows 5–7—results of test 1

Test 1 is performed with all seven circumferential rows of micro-structures, to provide information on the effect of rows 1–4 on micro-structure failures in rows 5–7. Different stress levels are given for each row by increasing applied forces with radial position, which are produced by circumferential velocities which increase with radius as they are induced by the rotating test chuck. These then should result in larger magnitudes of fluid shear force and form drag on individual structures as radial position increases. Centrifugal forces on individual structures are relatively small compared to these forces, as mentioned. Corresponding per cent failure and revolutions to failure data from test 1 for rows 5, 6 and 7 are presented in figure 10. According to this figure, the first group of failures, on the bottom left region of figure 10 (three failures from row 5, three failures from row 7) occur around 10 000 revolutions, and do not follow the later trend of failures. These failures are likely due to manufacturing defects, imperfections in the micro-structures, or incomplete adhesion to the stainless steel substrate. The remaining data in figure 10 follow trends which are different from earlier data (from tests 2 and 3) since the structures in row 5 fail before those in row 7. In addition, magnitudes of revolutions to failure are higher than observed with tests 2 and 3. The likely explanation for this effect is the effect of vapor bubbles that are intermittently present near rows 5, 6 and 7.

The presence of a vapor bubble is observed at a location near the center of the narrow gap of fluid between the test chuck and flat plate at a rotational speed of 3000 rpm. The presence and location of this bubble are due to higher static pressure at the outer edge and lower static pressure near the center of the narrow gap of fluid. In Test 1, passing structures, secondary flows, occasionally cause small vapor bubbles to break away from the main vapor bubble to be redistributed

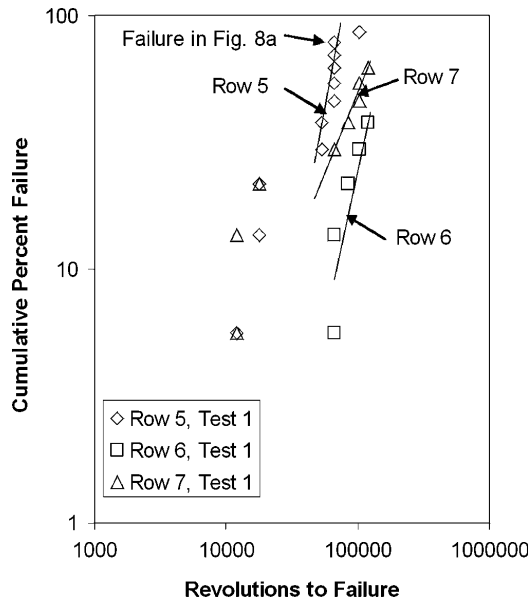


**Figure 10.** Micro-structure failure data for rows 5, 6 and 7 from test 1 for a test chuck rotational speed of 3000 rpm, and a small flow passage gap of 0.33 mm.

outward in a pulsating manner, such that they are intermittently present near rows 5, 6 and 7. The observed vapor bubbles near rows 5, 6 and 7 are small (estimated to be less than 0.1 mm in diameter). In addition to the small vapor bubbles near row 5, larger (1 to 2 mm in diameter) vapor bubbles are also observed near row 5. Considering the flow model of a cylinder in cross-flow described earlier, the presence of small vapor bubbles can decrease the total drag force of a cylinder in cross-flow by as much as 50% [32, 33]. The net effects of the small vapor regions are altered magnitudes of micro-structure loading, and additional alteration and damping of flow unsteadiness induced by the multiple circumferential rows of structures, which results in the higher revolutions to failure of row 6 and 7. The presence of a large vapor bubble near row 5 creates a pressure impulse to the micro-structure as the micro-structure passes through a sudden change in fluid density between the vapor bubble and the oil. This sudden increase in loading due to a pressure impulse generates larger momentary maximum stresses than predicted from the steady-state numerical modeling [34], thereby causing the micro-structures in row 5 to fail before rows 6 and 7. Overall, test 1 indicates that micro-structures near smaller inner radii may introduce additional flow phenomena that change the predicted behavior of the test. With this in mind, micro-structures should not be included near the center of the test chuck.

In spite of these differences in failure rates and failure times compared to tests 2 and 3, the most common mode of failure in test 1 is the same. In all cases, failures generally appear to begin with initial delamination initiating from one of the corners where local stresses are concentrated, followed by crack propagation, and then, a brittle fracture of the SU-8 photoresist micro-structures. Note that the data point associated with the structural failure shown in figure 8(a) is identified in figure 10. This is associated with the second to last failure on row 5 in figure 10.

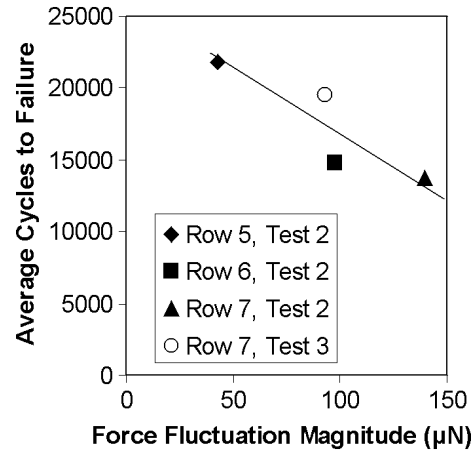


**Figure 11.** Average number of cycles to failure as dependent upon fluctuation magnitudes of total drag force applied to micro-structures for tests 2 and 3, where the total drag force is the sum of drag forces due to fluid shear, and pressure form drag.

#### 6.5. Average cycles to failure as affected by fluctuation magnitudes of total drag force

Figure 11 shows average cycles to failure as it depends upon the average peak-to-peak fluctuation magnitudes of total drag force applied to the micro-structures. The average peak-to-peak fluctuation magnitudes are determined by taking the average peak-to-peak variation of  $C_d$  with time from the numerical analysis presented by Braza *et al* [26] for Reynolds numbers from 100 to 1000. The total drag force fluctuations for row 7 of test 3 and row 5 of test 2 are due to Karman vortex shedding only, with no unsteadiness from the wakes of micro-structures at smaller radii. This is because no micro-structure rows exist at smaller radii for these micro-structure rows and test sequences. The magnitude of the force fluctuations is about five times smaller than the magnitude of the total steady drag force applied to each micro-structure, as discussed in section 4. Note that figure 11 shows that the average cycles to failure from row 7 from test 3 is greater than row 7 from test 2.

The peak-to-peak force fluctuation magnitudes are reported to increase due to the presence of wakes [28, 30], as discussed in section 4. The increase in fluctuation magnitudes for rows 6 and 7 of test 2, due to the Karman vortex shedding and unsteadiness from wakes of micro-structures at inner radii are estimated using the relationship of drag force fluctuation magnitude to average cycles to failure from row 7 of test 3 and row 5 of test 2, along with the increase of fluctuation magnitudes due to the presence of wakes [28, 30]. These fluctuation magnitudes are estimated to be 98  $\mu\text{N}$  and 140  $\mu\text{N}$ , respectively, which represent a 50% increase in fluctuation magnitude relative to fluctuation magnitudes without unsteady flow due to wakes from micro-structures at smaller radii.

Figure 11 shows that the average cycles to failure decrease as the force fluctuation magnitudes increase. Note that the average cycles to failure from row 7 from test 3 is greater than row 7 from test 2, providing additional indications of the influences of unsteady loading from wakes of micro-structures at smaller radii on failure of the micro-structures (when no vapor bubbles are present in the vicinity of the structural rows under observation).

## 7. Summary and conclusions

Presented is a procedure for failure characterization of micro-mechanical structures using a rotating Couette flow in a small gap. The test set-up is straight forward and inexpensive, and allows simultaneous testing of multiple micro-mechanical structures with different magnitudes of loading. This loading variation is provided by increasing applied forces with radial position produced by circumferential velocities which increase with radius as they are induced by the rotating test chuck. These velocities then result in larger magnitudes of fluid shear force and form drag on individual structures as radius increases. The estimated magnitude of the fluctuations in total drag force also increase with radial position due to vortex shedding. These are the dominant loading mechanisms when no unsteady forces from wakes from structures at smaller radii are present, and can be adjusted by changing the gap height or the rotational speed of the test chuck. The unsteady forces due to vortex shedding can be reduced or eliminated when testing smaller micro-structures, or flat layers. For larger or smaller gap heights, other phenomena may be present which may change flow behavior and structure loading to give different dependence on steady and unsteady applied forces.

As an example, this technique is employed to characterize the failure of arrays of SU-8 photoresist micro-structures placed on one or more circumferential rows on a 304 stainless steel test chuck. The results of these tests with multiple circumferential rows of micro-structures show that the presence of wake induced unsteadiness from micro-structures located upstream at smaller radii decrease the average cycles to failure by 30%. In all the test arrangements employed, the most common failure mode is a delamination at one of the corners of an individual SU-8 photoresist micro-structure, followed by crack propagation, and then, brittle structural fracture. A numerical structure model confirms the initial delamination location since it shows that the highest micro-structure stress concentrations are located near the four corners of the micro-structure, and across the bottom of the leading and trailing edges of the micro-structure.

The present technique can be used for comparative studies when optimizing fabrication processes for a particular micro-mechanical structure geometry. It is especially ideal for testing roughness elements and protrusions [17], structures on the surface of a flow passage [18] and adhesion between micro-fabricated structures and their substrate [19]. The method presented could be altered to test flat or thin layers, which gives an arrangement in which fluid shear forces are dominant, and form drag, centrifugal forces and unsteady loading are insignificant. With this arrangement, the modified technique can be employed to test common silicon micro-structures, the adhesion strength of micro-fabricated layers as well as other micro-mechanical structures and material systems.

## Acknowledgments

Mr James Stephenson and Mr Justin Millis are acknowledged for their assistance in the set-up and testing of the micro-structures. Support for this effort is provided by the National Science Foundation (NSF) through the IGERT Program at the University of Utah, Grant Number DGE 9987616.

## References

- [1] Amagi M 1995 Polyimide fatigue induced chip surface damage in DRAM's lead-on-chip (LOC) packages *Proc. 33rd Annu. 1995 IEEE Reliab. Phys. Symp.* pp 97–106
- [2] Park T S and Lee S B 2001 Mechanical fatigue tests of solder joint under mixed-mode loading cases *Proc. Int. Symp. Electron. Mater. Packag.* pp 438–43
- [3] Ogawa H, Suzuki K, Kaneko S, Nakano Y, Ishikawa Y and Kitahara T 1997 Measurements of mechanical properties of microfabricated thin films *Proc. IEEE Micro Electron. Mech. Syst. (MEMS)* pp 430–5
- [4] Cho H S, Hemker K J, Lian K and Goettart J 2002 Tensile, creep and fatigue properties of LIGA nickel structures *Proc. IEEE Micro Electron. Mech. Syst. (MEMS)* pp 439–42
- [5] Tsuchiya T, Tabata O, Sakata J and Taga Y 1996 Specimen size effect on tensile strength of surface-micromachined polycrystalline silicon thin films *J. Microelectromech. Syst.* **7** 106–13
- [6] Haque M A and Saif M T A 2001 Microscale materials testing using MEMS actuators *J. Microelectromech. Syst.* **10** 146–52
- [7] Haque M A and Saif M T A 2003 A review of MEMS-based microscale and nanoscale tensile and bending testing *Exp. Mech.* **43** 248–55
- [8] Ye X, Zhu J, Lu X, Zhou Z and Zhuo Y 2001 Measurement of the fracture property of polysilicon micro structure *J. Mech. Strength* **23** 443–6
- [9] Khoo H S, Liu K K and Tseng F G 2003 Mechanical strength and interfacial failure analysis of cantilevered SU-8 microposts *J. Micromech. Microeng.* **13** 822–31
- [10] Maekawa S, Takashima K, Shimojo M, Higo Y, Sugiura S, Pfister B and Swain M V 1999 Fatigue tests of Ni–P amorphous alloy microcantilever beams *Proc. Microprocesses Nanotechnol. Conf.* pp 132–3
- [11] Larsen K P, Ravnkilde J T, Ginnerup M and Hasen O 2002 Devices for fatigue testing of electroplated nickel (MEMS) *Proc. IEEE Micro Electron. Mech. Syst. (MEMS)* pp 443–6
- [12] Espinosa H D, Prorok B C and Fischer M 2003 A methodology for determining mechanical properties of freestanding thin films and MEMS materials *J. Mech. Phys. Solids* **51** 47–67
- [13] Park J H 2002 Development of micromechanical testing machine and its application *IEEE Trans. Compon. Packag. Manuf. Technol. A* **25** 317–32
- [14] Tu P L, Chang Y C, Hung K C and Lai J K L 2000 Comparative study of micro-BGA reliability under bending stress *IEEE Trans. Compon. Packag. Manuf. Technol. B* **23** 750–6
- [15] Saif M T A and MacDonald N C 1996 Micro mechanical single crystal silicon fracture studies torsion and bending *Proc. IEEE Micro Electron. Mech. Syst. (MEMS)* pp 105–9
- [16] Dai X, Brillhart M V and Ho P S 2000 Adhesion measurement for electronic packaging applications using double cantilever beam method *IEEE Trans. Compon. Packag. Manuf. Technol. A* **23** 101–16
- [17] Mottahed B and Molki M 1996 Artificial roughness effects on turbulent transfer coefficients in the entrance region of a circular tube *Int. J. Heat Mass Transfer* **39** 2515–23
- [18] Kim D S, Lee S W, Kwon T H and Lee S S 2003 Barrier embedded chaotic micromixer *Proc. IEEE Micro Electron. Mech. Syst. (MEMS)* pp 339–42
- [19] Chang-Yen D A, Lvov Y, McShane M J and Gale B K 2002 Electrostatic self-assembly of a ruthenium based oxygen sensitive dye using polyion-dye interpolyelectrolyte formation *Sensors Actuators B* **87** 336–45
- [20] Altin R, Cetinkaya S and Yucsu H S 2001 The potential of using vegetable oil fuels as fuel for diesel engines *Energy Convers. Manage.* **42** 529–38
- [21] Dellmann L, Roth S, Beuret C, Racine G A, Lorenz H, Despont M, Renaud P, Vettiger P and de Rooij N F 1997 Fabrication process of high aspect ratio elastic structures for

- piezoelectric motor applications *Proc. Int. Conf. Solid-State Sensors Actuators* pp 641–4
- [22] McAleavey A, Coles G, Edwards R L and Sharpe W N Jr 1999 Mechanical properties of SU-8 *Proc. Mater. Res. Soc. Symp.* **546** 213–8
- [23] MicroChem 2002 Nano<sup>TM</sup> SU-8: *Negative Tone Photoresist Formulation 50-100* (MicroChem, Newton, MA) Online at: [http://www.microchem.com/products/pdf/SU8\\_50-100.pdf](http://www.microchem.com/products/pdf/SU8_50-100.pdf)
- [24] Panton R L 1996 *Incompressible Flow* 2nd edn (New York: Wiley) pp 164–6
- [25] Schlichting H 1987 *Boundary Layer Theory* 7th edn (New York: McGraw-Hill) pp 15–32
- [26] Braza M, Chassaing P and Ha Minh G 1986 Numerical study and physical analysis of pressure and velocity fields in the near wake of a circular cylinder *J. Fluid Mech.* **165** 79–130
- [27] Baban F and So R M C 1991 Aspect ratio effect on flow-induced forces on circular cylinders in a cross-flow *Exp. Fluids* **10** 313–21
- [28] King R 1976 Wake interaction experiments with two flexible circular cylinders in flowing water *J. Sound Vib.* **45** 259–83
- [29] Nagai S and Kurata K 1971 Interference between cylinders in an open channel flow *Trans. Japan. Soc. Civil Eng.* **3** 200–1
- [30] Lam K, Li J Y and So R M C 2003 Force coefficients and Strouhal numbers of four cylinders in cross flow *J. Fluids Struct.* **18** 305–24
- [31] Ratner S B and Potapova L B 1991 Multicycle fatigue resistance of brittle polymers *Mech. Compos. Mater.* **26** 463–7
- [32] Yokosawa M, Kozawa Y, Inoue A and Aoki S 1986 Studies on two-phase cross flow: Part II. Transition Reynolds number and drag coefficient *Int. J. Multiph. Flow* **12** 169–84
- [33] Uchiyama T 1999 Numerical simulation of gas–liquid two-phase flow around a rectangular cylinder by the incompressible two-fluid model *Nucl. Sci. Eng.* **133** 92–105
- [34] Benham P P, Crawford R J and Armstrong C G 1996 *Mechanics of Engineering Materials* 2nd edn (Harlow, UK: Longman Group) pp 94–7